# Numerical simulation of the swirling flow of a finitely extensible non-linear elastic Peterlin fluid

Cite as: Phys. Fluids **32**, 103101 (2020); https://doi.org/10.1063/5.0021469 Submitted: 13 July 2020 . Accepted: 10 September 2020 . Published Online: 01 October 2020

Krishna T. Khambhampati 🗓, and Robert A. Handler 🗓









**Physics of Fluids** Special Issue on the Lattice Boltzmann Method

## Numerical simulation of the swirling flow of a finitely extensible non-linear elastic Peterlin fluid

Cite as: Phys. Fluids 32, 103101 (2020); doi: 10.1063/5.0021469 Submitted: 13 July 2020 · Accepted: 10 September 2020 ·







**Published Online: 1 October 2020** 







#### **AFFILIATIONS**

- Department of Mechanical Engineering, Texas A&M University, College Station, Texas 77843, USA
- <sup>2</sup>Department of Mechanical Engineering, George Mason University, Fairfax, Virginia 22030, USA
- a) Author to whom correspondence should be addressed: tejasvikrishna@gmail.com
- b) Electronic mail: rhandler@gmu.edu

#### **ABSTRACT**

Viscoelastic fluids have been shown to undergo instabilities even at very low Reynolds numbers, and these instabilities can give rise to a phenomenon called elastic turbulence. This phenomenon, observed experimentally in viscoelastic polymer solutions, is driven by the strong coupling between the fluid velocity and the elasticity of the flow. To explore the emergence of these instabilities in a viscoelastic flow, we have chosen to explore, by means of direct numerical simulations, a particular case called von Kármán swirling flow. The simulations employ the finitely extensible nonlinear Peterlin model to represent the dynamics of a dilute polymer solution. Notably, a log-conformation technique is used to solve the governing equations. This method is useful in overcoming the high Weissenberg number problem. The results obtained from the simulations were generally in good agreement with experiments. The torque on the top plate was decomposed into Newtonian and polymeric components, and it was found that the polymeric component was dominant. In addition, flow visualizations revealed that a toroidal vortex was strongly correlated with the distribution of the stresses on the rotating plate.

Published under license by AIP Publishing. https://doi.org/10.1063/5.0021469

#### I. INTRODUCTION

Experiments have revealed a new phenomenon that has been referred to as elastic turbulence. This flow phenomenon was first discovered in the swirling flow of a dilute polymer solution driven by a rotating plate. The torque on the plate was found to be roughly one order of magnitude greater than the corresponding torque in the flow of a Newtonian fluid. It is the primary objective of this work to perform direct numerical simulations (DNSs) of the exact same flow with comparable fluid properties and geometry. DNS methods such as those used in this work can reveal information that cannot be easily obtained experimentally, such as the entire fluid velocity field in space and time as well as the internal stress fields. Furthermore, the correlation between the velocity field and other quantities such as stress can be investigated in detail. The methods described in this work allow us to more deeply investigate this flow and offer an opportunity to gain greater insight into the instabilities found in viscoelastic flows. To place the current work in context, we first review

the relevant literature concerning instabilities in flows of polymer solutions, elastic turbulence, and swirling flows as well as the primary model used in this work, the finitely extensible non-linear elastic Peterlin (FENE-P) model.

## A. Instabilities in dilute polymer solutions

In this work, we focus on fluids with intrinsic elasticity, commonly referred to as viscoelastic fluids. Most viscoelastic fluids are either composed of polymers (polymer melts) or contain polymers (polymer solutions). Specifically, the work presented here involves dilute-polymer solutions, which are a particular subclass of viscoelastic fluids. Before turning our attention to the instabilities caused by fluid elasticity, it is useful to make a note of the phenomenon of turbulent drag reduction that occurs at high Reynolds numbers in viscoelastic fluids. In 1948, Toms<sup>2</sup> reported that using a solution consisting of a minute amount of a high molecular weight

polymer dissolved in water can substantially reduce friction drag compared with that of the pure solvent, in a high Reynolds number pipe flow. Since that time, a vast amount of research has been performed to elucidate the mechanism of drag reduction by polymer addition.<sup>3-5</sup> However, it has been found that polymer additives can have significant effects also in low Reynolds number flows. For example, instabilities solely due to the inherent elasticity of the fluid have been discovered in a wide number of flows over roughly the past three decades.6-20

Until recently, elastic instabilities have been found to occur primarily in geometries with curved rather than rectilinear mean streamlines. It has been found that a key component in characterizing the development of these elastic instabilities is the Weissenberg number  $Wi = \frac{\lambda V}{L}$ , where V is a characteristic velocity scale, L is a characteristic length scale, and  $\lambda$  is the polymeric relaxation time. When the Weissenberg number is greater than a critical value, instabilities typically appear and involve a sharp growth in local elastic stress as a result of the extensibility of the polymers. This occurs as the relaxation time scale becomes on the order of the rate of deformation. The sharp growth in elastic stress is accompanied by the emergence of velocity fluctuations in the flow. In Fig. 1, different regimes characterized by varying Weissenberg and Reynolds numbers are shown. Note that the term "inertial turbulence" is used here to refer to turbulent flows in Newtonian fluids such as in pipe, channel, and boundary layer flows at higher Reynolds numbers, where the sources of nonlinearity are inertial forces, as distinguished from elastic turbulence, where the dominant source of nonlinearity is derived from elastic stresses.

#### B. Elastic turbulence

The phenomenon called elastic turbulence can be roughly defined as a chaotic low Reynolds number flow that develops

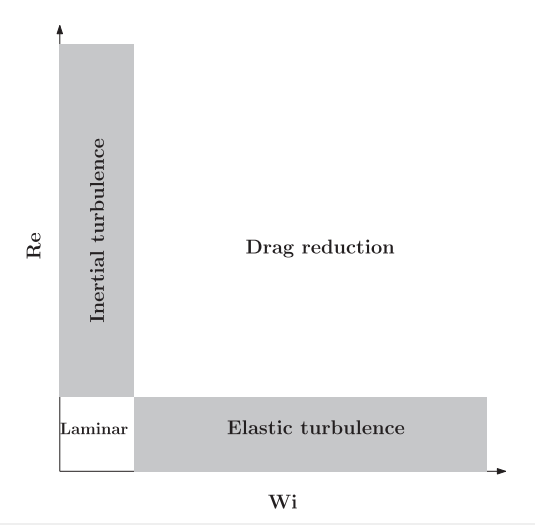


FIG. 1. Flow regimes in the Weissenberg–Reynolds number (Wi–Re) space. At low Weissenberg number ( $Wi = \lambda V/L$ ) and low Reynolds number ( $Re = VL/\nu$ ), the flow is laminar. At low Wi and high Re, the flow becomes classical inertial turbulence. At high Wi and high Re, the flow exhibits the drag reduction phenomenon. At high Wi and low Re, elastic turbulence is observed.

from elastic instabilities. The initial discovery of elastic turbulence was followed by a number of other experimental investigations in which it was found not only in swirling flow<sup>22,23</sup> but also in Taylor-Coutte flow<sup>24</sup> and Dean flow.<sup>24-27</sup> We have previously remarked that all the flows cited above were those with curved streamlines. However, recent experiments<sup>28,29</sup> have revealed instabilities in viscoelastic flows within micro-channels with rectilinear streamlines. In all of these flows, a wide range of length scales are excited, accompanied by a significant increase in momentum transport, comparable to that found in turbulent flows of Newtonian fluids.

In elastic turbulence, the energy spectrum of the velocity fluctuations is found to behave as  $E(k) \approx k^{-n}$ , where E is the spectral energy density of the velocity fluctuations, k is the wavenumber, and n is typically found to be about 3.5. This steep drop-off in the energy spectrum should be compared to the much smaller n = 5/3 found in classical inertial turbulence. Despite some differences between elastic turbulence and standard high Reynolds number inertial turbulence, elastic turbulence gives rise to significant increases in transport well above the laminar state, and for this reason, it remains intriguing as a possible means of increasing the flux of mass, momentum, and heat in flow devices that are not large enough to develop ordinary inertial turbulence.

The numerical simulation of elastic turbulence is challenging for numerous reasons. The biggest hurdle is dealing with numerical convergence issues at high Wi. Specifically, numerical breakdown occurs when solving the FENE-P model (or any another model that involves hyperbolic PDEs). However, elastic instabilities and elastic turbulence are reported to occur only at higher Wi. This numerical breakdown that occurs at moderately high Weissenberg numbers is called the High Weissenberg Number Problem (HWNP). There are two primary reasons for this breakdown. The first is the inability of polynomial-based approximations to represent the steep spatial gradients of the conformation tensor.<sup>30</sup> Second, there is frequently a loss of positive definiteness of the conformation tensor.<sup>30</sup> Due to the so-called "HWNP," most numerical simulations in the literature have been restricted to rectilinear geometries and limited parameter ranges. 31-33 However, Liu and Khomami<sup>34</sup> performed a DNS of viscoelastic Taylor-Couette flow and reported the exponential decay of the time scales, as reported in the experiments.

#### C. Swirling flows

Swirling flows are ubiquitous both in nature and technology. Large rotating flows are found both in the atmosphere and oceans, whereas industrial applications of swirling flows are associated with turbines and centrifugal pumps, among others. A special case of such a flow is that between two coaxial rotating plates or disks.

The flow of an incompressible fluid driven by an infinite rotating disk in an unbounded fluid domain is a classical problem in fluid mechanics. von Kármán<sup>35</sup> was the first to study this problem for Newtonian fluids by using a transformation that reduced the Navier-Stokes equations to a set of ordinary differential equations. Mitschka<sup>36</sup> showed that von Kármán's similarity solution could be extended to power-law fluids. Ariel<sup>37</sup> showed that a similarity solution does exist for a particular class of viscoelastic swirling flows in unbounded domains.

The first attempt to investigate the effects of viscoelasticity on confined swirling flows of viscoelastic fluids was made by Stokes et al. 38 They observed some unsteady flow patterns by using a polyacrylamide Boger fluid<sup>39</sup> with relatively high viscosity, which minimized the inertial effects in the flow. By picking a polymer solution with a high viscosity, they inferred that the observed non-Newtonian effects were purely elastic in nature. On the other hand, when the fluid used is a low viscosity dilute polymer solution such that inertial effects could not be ignored, they observed that the stress increase on the rotating plate that is attributed to turbulent drag is delayed. In some extreme cases, the stress increase is suppressed due to the presence of the polymer. They reported that swirling flows became unstable for both inertia dominated flows (high Re, low Wi) and elasticity dominated flows (low Re, high Wi). Thus, they found an extremely strong correlation between the ratio Wi/Re and the type of instability that emerged in the flow. This ratio is referred to as the elasticity number El. Hence, in short, the flow is dominated by elastic effects when  $El \ge 1$ , and if El < 1, the flow becomes inertia dominated.

The flow between two rotating plates is of considerable importance and forms the basis for rheological measurements of viscosity and normal stresses in both Newtonian and non-Newtonian liquids. Some extrusion processes of polymers also employ such flow geometries. The simplest case of this flow geometry consists of two coaxial disks, separated by a small distance. In a typical rheological measurement, fluid samples are contained in the narrow gap and are subject to the rotation of the upper plate at a constant angular velocity, while the bottom plate is kept fixed. This experimental setup is of particular importance since it was also used by Groisman and Steinberg<sup>1</sup> to uncover the elastic turbulence phenomenon.

## D. The FENE-P model and its applications

Maxwell<sup>40</sup> is credited with developing viscoelastic models based on appealing to ideas that stem from the kinetic theory of gases. Warner<sup>41</sup> appealing to spring-dashpot-dumbbell analogs developed by Bird and Warner<sup>42</sup> introduced a model that is referred to as the finitely extensible non-linearly elastic model, often referred to as the FENE model. The FENE-P model uses the work of Peterlin<sup>43</sup> to provide closure to the FENE model and is used often in modeling non-Newtonian fluids.

In this work, we have chosen to use the FENE-P model to represent the polymer dynamics. 44,45 In the FENE-P model, the solvent is viewed as being populated with large numbers of linear polymer molecules, each of which is thought of as a dumbbell consisting of two massless spheres, connected by a non-linear spring. The solvent flow can affect the stretch and orientation of the dumbbells due to viscous forces. The dumbbells act back on the fluid, thus coupling the polymeric effects directly to fluid motions. In this approach, the dumbbells are prevented from stretching to infinite lengths by introducing the nonlinear spring model through the Peterlin function.

The FENE-P model has proven effective in recent years in exploring complex phenomena such as the effect of polymer additives in fully turbulent flows, although some unrealistic aspects of the model have been discussed in recent work. High resolution direct numerical simulations (DNSs) 47-51 of such flows have confirmed the experimental observations of Toms<sup>2</sup> and others. At These

simulations have shown that the drag reduction phenomenon can be replicated by coupling the polymeric forces modeled as Peterlin dumbbells with the equations of fluid motion. In addition, for use in simulating turbulent high Reynolds number polymeric flows, the FENE-P model has recently been incorporated into Reynolds-averaged Navier–Stokes models<sup>51–53</sup> and k-epsilon turbulence models<sup>54–56</sup> and has been used to study the effects of polymers on heat transfer.<sup>57</sup> The model has also been used with success in exploring the physics of low Reynolds number flows.<sup>33,34,58</sup> The FENE-P model has also been used to show that coherent vorticity can be generated in dilute polymer solutions.<sup>59</sup>

### E. Outline of the paper

This paper is organized as follows: In Sec. II, we describe the geometry, the boundary conditions, the viscoelastic constants, the definitions of the relevant non-dimensional numbers, and the mathematical formulation of the problem. In Sec. III, we describe the log-conformation reformulation (LCR) technique, the implementation of this method in ANSYS-FLUENT, the mesh, and the simulation parameters. In Sec. IV, we present results from two different kinds of simulations that we refer to as constant- $\Omega$  and ramp-up. In Sec. V, we give an overview of this work and offer suggestions for future efforts.

#### II. PROBLEM FORMULATION

#### A. Mathematical formulation

The problem of interest is governed by the momentum equation and the continuity equation for an incompressible fluid given, respectively, by

$$\rho \frac{D\mathbf{u}}{Dt} = -\nabla p + \nabla \cdot \mathbf{S} \tag{1}$$

and

$$\nabla \cdot \boldsymbol{u} = 0, \tag{2}$$

where  $\boldsymbol{u}$  is the fluid velocity, p is the pressure,  $\boldsymbol{S}$  is the stress tensor, and  $\rho$  is the density. For a dilute polymer solution, the stress is decomposed into Newtonian and polymeric components via

$$\mathbf{S} = 2\mu_0 \beta \mathbf{D} + \boldsymbol{\sigma}^P,\tag{3}$$

where  $\sigma^P$  is the polymeric component of the stress,  $\mu_0$  is the solution viscosity,  $\beta$  is the ratio of the solvent viscosity to the solution viscosity, and D is the symmetric part of the velocity gradient tensor. For a FENE-P fluid, the polymeric stress is given by

$$\boldsymbol{\sigma}^{P} = \frac{\mu_0(1-\beta)}{\lambda} [f(R)\boldsymbol{C} - \boldsymbol{I}]. \tag{4}$$

Here,  $\lambda$  is the polymer relaxation time, C is the conformation tensor defined as the average over all possible molecular configurations of the product of the end-to-end vectors associated with the polymer,  $R^2 = \operatorname{tr}(C)$ , I is the unit tensor, and  $f(R) = \frac{L_0^2 - 3}{L_0^2 - R^2}$  is the Peterlin function, where  $L_0$  is the maximum allowable molecular extension. In the equations above, and in all subsequent ones, C,  $L_0$ , and R are made non-dimensional by the rest length, or square of the length as appropriate, of the polymer molecule. Finally, the conformation tensor C is governed by

$$\frac{DC}{Dt} = (\nabla u)C + C(\nabla u)^{T} - \frac{1}{\lambda}[f(R)C - I].$$
 (5)

## B. Geometry, boundary conditions, and coordinate systems

The geometry of the swirling flow that we are concerned with in this work is given in Fig. 2. The flow system consists of a fixed enclosed circular cylinder of radius  $R_o$  and depth D with a lid whose radius is  $R_i$ . This lid is set to rotate with a constant angular velocity  $\Omega$ . The bottom disk and the side wall are assumed to be at rest. A no-slip boundary condition on the velocity and a no-flux boundary condition on the components of  $\mathbf{C}^{60}$  have been imposed along all boundary surfaces.

In this work, we will use two coordinate systems. The first is the Cartesian system (x, y, z) and the second is the cylindrical coordinate system  $(r, \theta, x)$ , which are described relative to the geometry in Fig. 2. The unit vectors in these systems are  $\hat{x}$ ,  $\hat{y}$ ,  $\hat{z}$  and  $\hat{r}$ ,  $\hat{\theta}$ ,  $\hat{x}$ , respectively. In addition, the fluid velocity vector  $\boldsymbol{u}$  has components  $u_x$ ,  $u_y$ ,  $u_z$  and  $u_r$ ,  $u_\theta$ ,  $u_x$  in these systems.

#### C. Parameter values and non-dimensional numbers

In all simulations,  $R_o = 43.6$  mm, D = 10 mm, and  $R_i = 38$  mm. The fluid properties used in the simulation are as follows: the density of the fluid is  $\rho = 4240$  kg/m³, the viscosity of the solvent is  $\mu_s = 0.324$  Pa s, the viscosity of the solution is  $\mu_0 = 0.424$  Pa s, and the relaxation time is given by  $\lambda = 3.4$  s. In addition,  $\beta = \mu_s/\mu_0 = 0.764$ , and the maximum polymer length,  $L_0$ , was set to 100. All values of the physical properties of the fluid cited above are identical to those used in the experiments by Groisman and Steinberg. In describing the results of these simulations, it is useful to define several non-dimensional parameters. The Weissenberg number, which is defined as the ratio between the relaxation time scale to the shear time scale, is given by  $Wi = \lambda \Omega R_i/D$ , the Reynolds number is defined as  $Re = (\rho \Omega R_i D)/\mu_0$ , and the shear rate is defined by  $\dot{\gamma} = \Omega R_i/D$ . The elasticity number is defined as  $El = Wi/Re = \lambda \mu_0/\rho D^2$ .

#### **III. NUMERICAL METHODS**

The phrase "High Weissenberg Numerical Problem" (HWNP) was coined to describe the common situation experienced by researchers in which numerical simulations failed beyond some limiting value of the Weissenberg number. 30,61,62 This limiting value varies with the flow geometry and the fluid constitutive model used

in a given problem. As previously mentioned, it is generally recognized that the HWNP stems from the loss of the symmetric positive definiteness (SPD) of the conformation tensor, and also the inability of a low-order polynomial fitting to capture the steepest gradients of the components of the conformation tensor.

Much effort has been devoted toward resolving the HWNP. Vaithianathan and Collins<sup>61</sup> proposed a decomposition algorithm for the conformation tensor to guarantee SPD and improve the overall stability of the simulation. Fattal and Kupferman<sup>30,62</sup> proposed formulating the equations in terms of the logarithm of the conformation tensor, which is called the log-conformation reformulation (LCR). This method preserves the SPD of the conformation tensor. It also allows much more rapid convergence, which would otherwise cause the simulation to fail. This formulation has been successfully implemented for a flow around a cylinder,<sup>63</sup> lid-driven cavity,<sup>62</sup> and Poiseuille flow,<sup>64</sup> which indicates the advantage and validity of using the log-conformation reformulation for solving the HWNP.

#### A. The log-conformation reformulation

The LCR approach proposed by Fattal and Kupferman<sup>30</sup> is based on the idea that instead of solving the evolution equation for the conformation tensor C [see Eq. (5)], an evolution equation for the natural logarithm of the conformation tensor  $\phi = \log(C)$  is solved. This approach reduces the magnitude of the gradients of conformation tensor fields. Since C is an SPD matrix, it can be diagonalized as follows:

$$C = R\Lambda R^T, \tag{6}$$

where R is a matrix composed of the eigenvectors of C and  $\Lambda$  is a matrix in which the diagonal elements are the eigenvalues of C as follows:

$$\mathbf{\Lambda} = \begin{bmatrix} \lambda_1 & 0 & 0 \\ 0 & \lambda_2 & 0 \\ 0 & 0 & \lambda_3 \end{bmatrix}, \tag{7}$$

where  $\lambda_1$ ,  $\lambda_2$ , and  $\lambda_3$  are the real eigenvalues of C. The field  $\phi$  can be calculated by taking the logarithm of each element in the diagonal matrix<sup>30</sup> as follows:

$$\phi = \log(C) = R\log(\Lambda)R^{T}.$$
 (8)

For the purpose of reformulating Eq. (5), Fattal and Kupferman<sup>30</sup> show that for any incompressible fluid, the velocity gradient tensor

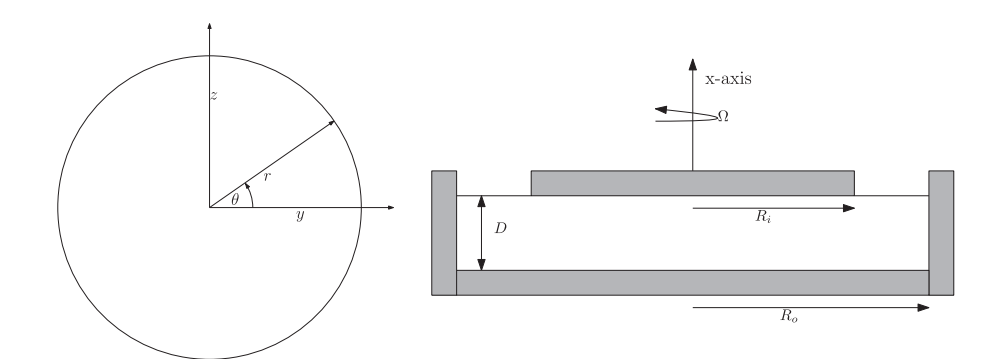


**FIG. 2.** The schematic of the system under investigation. The top view (on the left) of the system shows the coordinates, y and z, as well as r and  $\theta$ . The side view (on the right) shows the outer container whose radius and depth are  $R_0$  and D, respectively. Also shown is the top plate that rotates at an angular velocity  $\Omega$  and whose radius is  $R_i$ .

 $\nabla u$  can be decomposed as follows:

$$\nabla u = \Omega + B + NC^{-1}, \tag{9}$$

where  $\Omega$ , N, and B are defined as

$$\mathbf{\Omega} = \mathbf{R} \begin{bmatrix} 0 & \omega_1 & \omega_2 \\ -\omega_1 & 0 & \omega_3 \\ -\omega_2 & -\omega_3 & 0 \end{bmatrix} \mathbf{R}^T, \tag{10}$$

$$\boldsymbol{B} = \boldsymbol{R} \begin{bmatrix} m_{11} & 0 & 0 \\ 0 & m_{22} & 0 \\ 0 & 0 & m_{33} \end{bmatrix} \boldsymbol{R}^{T}, \tag{11}$$

$$\mathbf{N} = \mathbf{R} \begin{bmatrix} 0 & n_1 & n_2 \\ -n_1 & 0 & n_3 \\ -n_2 & -n_3 & 0 \end{bmatrix} \mathbf{R}^T$$
 (12)

with  $\omega_1 = \frac{\lambda_2 m_{12} + \lambda_1 m_{21}}{\lambda_2 - \lambda_1}$ ,  $\omega_2 = \frac{\lambda_3 m_{13} + \lambda_1 m_{31}}{\lambda_3 - \lambda_1}$ ,  $\omega_3 = \frac{\lambda_3 m_{23} + \lambda_2 m_{32}}{\lambda_3 - \lambda_2}$ ,  $n_1 = \frac{m_{12} + m_{21}}{\lambda_2^{-1} - \lambda_1^{-1}}$ ,  $n_2 = \frac{m_{13} + m_{31}}{\lambda_3^{-1} - \lambda_1^{-1}}$ ,  $n_3 = \frac{m_{23} + m_{32}}{\lambda_3^{-1} - \lambda_2^{-1}}$ , and the  $m_{ij}$ 's are defined as the elements of a matrix M defined by

$$\mathbf{M} = \mathbf{R}^T \nabla \mathbf{u} \mathbf{R} = \begin{bmatrix} m_{11} & m_{12} & m_{13} \\ m_{21} & m_{22} & m_{23} \\ m_{31} & m_{32} & m_{33} \end{bmatrix}.$$
(13)

Using the decomposition from Eq. (9), Eq. (5) can be rewritten as

$$\frac{DC}{Dt} = \Omega C - C\Omega + 2BC + \frac{1}{\lambda} [I - f(R)C]. \tag{14}$$

Referring to Eq. (8), the decomposed evolution equation (14) can be rewritten as follows:

$$\frac{D\phi}{Dt} = \Omega\phi - \phi\Omega + 2B + R \left[ \frac{1}{\lambda} (\Lambda^{-1} - f(R)I) \right] R^{T}.$$
 (15)

#### **B. Implementation using ANSYS-FLUENT**

The details of the algorithm are given in the flowchart shown in Fig. 3. The algorithm is a modification of the SIMPLE (Semi-Implicit Method for Pressure-Linked Equations) method. In this method, the governing equations are discretized in a strong-conservation form using a finite-volume approach. The non-linearities are computed in the "outer loop," which is performed several times per time step until satisfactory convergence is reached. In each iteration of the "outer loop," the momentum [Eq. (1)], mass [Eq. (2)], and modified version of the transport equation [Eq. (15)] are solved iteratively until a specified convergence criterion is satisfied.

Using the LCR approach, Eq. (15) is solved using the user-defined scalar transport functionality in ANSYS-FLUENT. This capability allows the user to solve an advective-diffusion equation for a scalar  $\psi$  of the following form:

$$\frac{\partial \rho \psi}{\partial t} + \frac{\partial}{\partial x_i} \left( \rho u_i \psi - \Gamma \frac{\partial \psi}{\partial x_i} \right) = S_{\psi}, \tag{16}$$

where  $\rho$  is the fluid density,  $u_i$  are the components of the fluid velocity,  $\Gamma$  is the diffusion coefficient, and  $S_{\psi}$  is a source term. Using this capability, the six unique components of  $\phi$  can be determined by allowing the source term  $S_{\psi}$  to represent the right-hand side of Eq. (15). After solving for  $\phi$ , the conformation tensor can be updated using Eqs. (6)–(8) and (13).

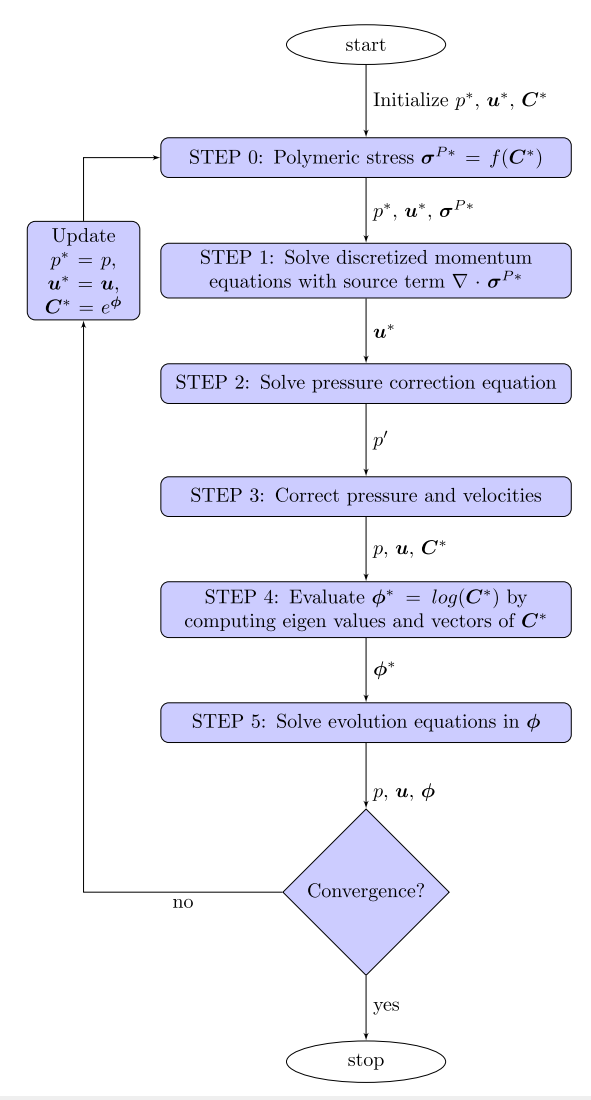


**FIG. 3**. Flowchart of the numerical algorithm. All the equations discussed in this work were implemented in ANSYS-FLUENT using user-defined functions. The implementation of the LCR algorithm requires a series of linear algebra operations including the evaluation of the eigenvalues of the conformation tensor. In order to achieve this, the Visual Studio C compiler has been configured such that it is accessible from ANSYS-FLUENT. This allowed the LAPACK routines to be utilized. The starred variables denote uncorrected variables within an iteration, whereas the un-starred variables represent the corrected variables.

## C. Mesh and simulation parameters

The mesh shown in Fig. 4, which has 22 344 tetrahedral cells, was created using a computational fluid dynamics (CFD) meshing software called ANSYS-ICEM. The domain has been divided into 14 sections parallel to the rotating disk with each section having 1596 elements. The total volume of the domain is 50 240 mm $^3$ . The minimum and maximum volume of the cells are 1.123 267 mm $^3$  and 3.955 476 mm $^3$ , respectively. The time step in every simulation was chosen to be  $10^{-2}$  s.

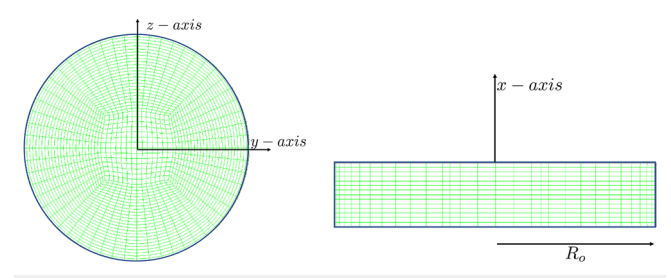


**FIG. 4.** The mesh used for the simulation has 22 344 tetrahedral cells and was created using a CFD meshing software called ANSYS-ICEM. The domain has been divided into 14 sections parallel to the rotating disk with each section having 1596 elements. The total volume of the domain is 50 240 mm<sup>3</sup>. The minimum and maximum volume of the cells are 1.123 267 mm<sup>3</sup> and 3.955 476 mm<sup>3</sup>, respectively. The top view of the mesh is shown on the left, and the side view is shown on the right.

#### **IV. RESULTS**

The primary goal of this work is to compare the results from our simulations with those of experiments. An important parameter of driven swirling flows is the torque Q that is required to drive the flow. The only component of the stress tensor T that contributes to the torque on the top plate is  $\tau_{\theta x}(r,\theta)$ . Therefore, the torque  $Q = Q\hat{x}$  can be computed as follows:

$$Q = \int rdF = \int_0^{R_i} \int_0^{2\pi} \sigma_{\theta x} r^2 d\theta dr$$
 (17)

since dF, which is the differential component of the force acting on the plate, is given by  $\sigma_{\theta x} r d\theta dr$ . It is convenient to define the average stress,  $T_{av}$ , on the top plate in terms of Q as follows:

$$T_{av} = \frac{3Q}{2\pi R_i^3}. (18)$$

It is evident that  $T_{av}$  represents the spatially uniform stress that would be required to generate the torque Q. We note that  $\sigma_{\theta x}$ , Q, and  $T_{av}$  are implicitly functions of time, t.

Before discussing the results from our simulations in detail, it is necessary to determine the highest Weissenberg number that can be accommodated using the LCR technique. This is achieved by carrying out a series of simulations (see the Appendix for a listing of all simulations performed in this work) with varying Wi. It was determined by performing these simulations that flows with a Weissenberg number < 24 could be successfully simulated. We performed two different types of simulations in this work, which we refer to as (A) constant  $\Omega$  simulations and (B) ramp-up simulations. In the constant  $\Omega$  simulations, the fluid was initially at rest and the rotation rate of the top plate,  $\Omega$ , was kept constant throughout the simulations. In the ramp-up simulations, the fluid was also initially at rest, but the rotation rate of the top plate was an increasing function of time, t, given by  $\Omega = 0.058t$ . From all the constant  $\Omega$ simulations, we have selected four cases (see Table I), which are most representative of all of them and can be most easily compared to experiments.

In order to discuss the simulations described above, it is necessary to define the notation used to describe the stresses acting on the top plate. For the purely Newtonian case, the case in which no

**TABLE I.** For each run, we list the angular velocity of the plate,  $\Omega$ , the shear rate,  $\dot{\gamma}$  (s<sup>-1</sup>), the Reynolds number, Re, and the Weissenberg number, Wi. In this table, we list only the runs that are discussed in the body of the paper. For a complete list of all runs, see the Appendix.

Run no.	$\Omega({\rm rad~s}^{-1})$	$\dot{\gamma}$ (s <sup>-1</sup> )	Re	Wi
1	0.71	2.7	2.7	9.18
2	1.05	4	4	13.6
3	1.55	5.9	5.9	20.06
4	1.76	6.7	6.7	22.78

polymer stresses exist, the average stress on the top plate as defined in Eq. (17) is denoted by  $T_N$ . This stress is determined for flows in which the parameter  $\beta=1$ . When  $\beta<1$ , the polymeric stresses are important. In such cases, we denote the average stress on the top plate to be  $T_V$ . It is clear from Eqs. (3) and (4) that  $T_V$  can be decomposed as  $T_V=\tau_P+\tau_N$ , where  $\tau_P$  and  $\tau_N$  are, respectively, the average polymeric and Newtonian stresses on the top plate. It is important to note that all conclusions reached in this work are based on the comprehensive set of simulations given in the Appendix.

### A. Constant $\Omega$ simulations

The constant  $\Omega$  simulations were those in which the rotation rate,  $\Omega$ , is kept constant throughout the entire time span of the simulations. In Figs. 5–7, we show, respectively, the time evolution of the stresses  $\tau_N$ ,  $\tau_P$ , and  $T_V$ . In each of these figures, results are shown for values of the shear rate,  $\dot{\gamma}=2.7~{\rm s}^{-1}$ ,  $4.0~{\rm s}^{-1}$ ,  $5.9~{\rm s}^{-1}$ , and  $6.7~{\rm s}^{-1}$ . It is clear from these results that after an initial transient period that lasts  $t\approx 20~{\rm s}$ , the flow reaches a steady-state or an oscillatory steady-state, depending on the value of  $\dot{\gamma}$ . For example, for  $\dot{\gamma}=2.7~{\rm s}^{-1}$  and  $\dot{\gamma}=4.0~{\rm s}^{-1}$ , a non-oscillatory steady-state is reached; however, for  $\dot{\gamma}=5.9~{\rm s}^{-1}$  and  $\dot{\gamma}=6.7~{\rm s}^{-1}$ , an oscillatory steady-state emerges. We also observe from these results that the contribution to the torque on the top plate from the polymeric component,  $\tau_P$ , is significantly larger than the contribution due the Newtonian component,  $\tau_N$ . A closer look at the oscillatory steady state for  $\dot{\gamma}=6.7~{\rm s}^{-1}$  is shown in Fig. 8.

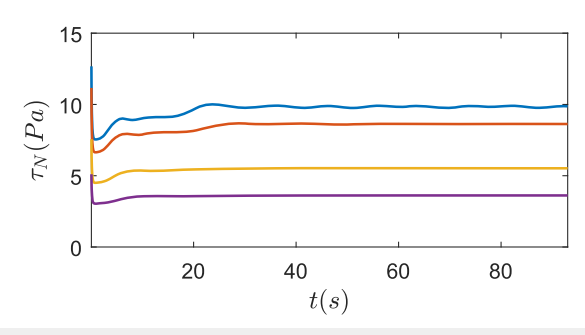


**FIG. 5**. The temporal evolution of the Newtonian component of the total average stress,  $\tau_N$ , for shear rates  $\dot{\gamma}$  = 2.7 s<sup>-1</sup>, 4.0 s<sup>-1</sup>, 5.9 s<sup>-1</sup>, and 6.7 s<sup>-1</sup>. The units for  $\tau_N$  are pascals. The curves for these shear rates are given, respectively, by the colors purple, yellow, red, and blue.

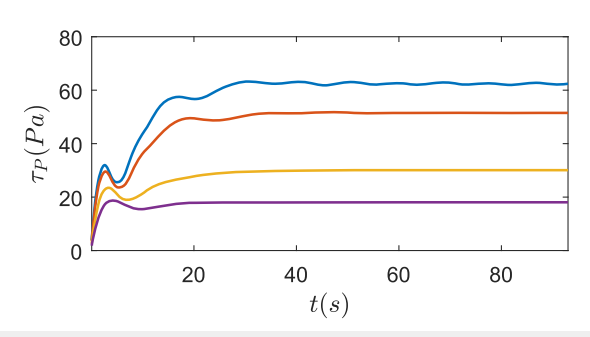


**FIG. 6.** The temporal evolution of the polymeric component of the total average stress,  $\tau_P$ , for shear rates  $\dot{\gamma}$  = 2.7 s<sup>-1</sup>, 4.0 s<sup>-1</sup>, 5.9 s<sup>-1</sup>, and 6.7 s<sup>-1</sup>. The curves for these shear rates are given, respectively, by the colors purple, yellow, red, and blue

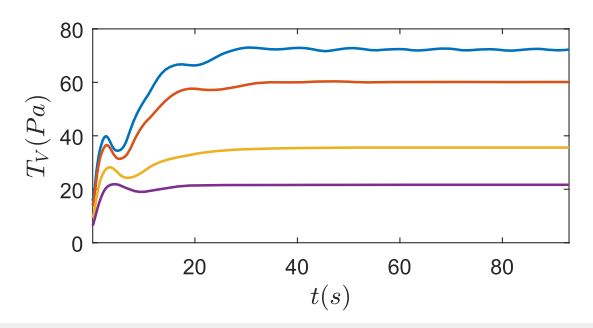


**FIG. 7**. The temporal evolution of the total average stress,  $T_V$ , for shear rates  $\dot{\gamma}$  = 2.7 s<sup>-1</sup>, 4.0 s<sup>-1</sup>, 5.9 s<sup>-1</sup>, and 6.7 s<sup>-1</sup>. The curves for these shear rates are given, respectively, by the colors purple, yellow, red, and blue.

In Fig. 9, the evolution of the total stress  $T_V$  normalized with Newtonian stress  $T_N$  is shown. We reiterate that  $T_N$  is the stress obtained from a purely Newtonian flow for which  $\beta=1$ . It is important to note that  $T_N$ , which we have used for normalization, has been obtained for exactly the same strain rate as in the corresponding non-Newtonian case. For example, in Fig. 9, the plot for  $T_V$  for  $\dot{\gamma}=6.7~{\rm s}^{-1}$  has been normalized with the stress  $T_N$  obtained from a Newtonian simulation for which  $\dot{\gamma}=6.7~{\rm s}^{-1}$ . It is clear from Fig. 9 that in all cases, the total stress  $T_V$  is significantly larger than  $T_N$ . Furthermore, for  $\dot{\gamma}=6.7~{\rm s}^{-1}$ ,  $T_V$  is nearly an order of magnitude

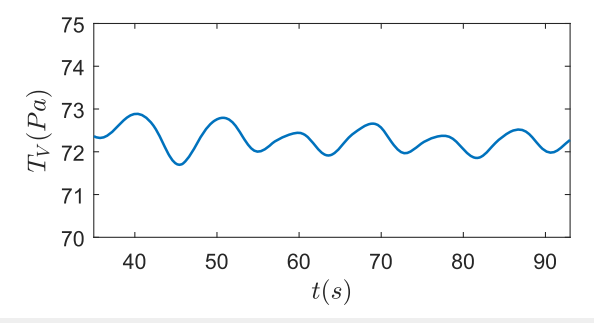


**FIG. 8**. The temporal evolution of the total average stress,  $T_V$ , for the shear rate  $\dot{\gamma}=6.7~{\rm s}^{-1}$  during the time period for which the flow is in a quasi-periodic steady-state.

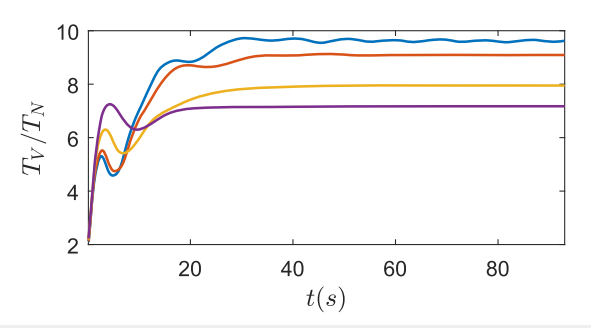


**FIG. 9**. The temporal evolution of the normalized average stress,  $T_V/T_N$ , for shear rates  $\dot{y}=2.7~{\rm s}^{-1}$ ,  $4.0~{\rm s}^{-1}$ ,  $5.9~{\rm s}^{-1}$ , and  $6.7~{\rm s}^{-1}$ . The curves for these shear rates are given, respectively, by the colors purple, yellow, red, and blue.

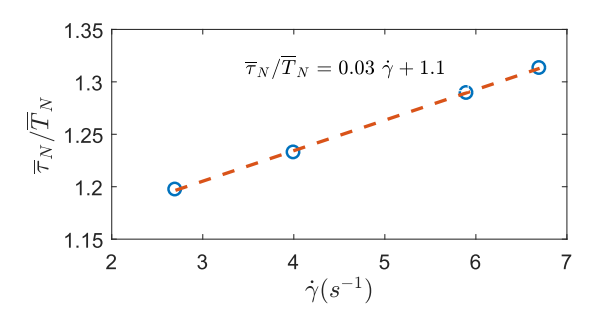


**FIG. 10.**  $\overline{\tau}_N/\overline{T}_N$  for shear rates  $\dot{\gamma}$  = 2.7 s<sup>-1</sup>, 4.0 s<sup>-1</sup>, 5.9 s<sup>-1</sup>, and 6.7 s<sup>-1</sup>. The equation of the line fit used is  $\overline{\tau}_N/\overline{T}_N = 0.029\dot{\gamma} + 1.1$ . The coefficient of determination is  $R^2$  = 0.9994.

greater than  $T_N$ . The dependence of the normalized time-averaged stresses  $\overline{\tau}_P$ ,  $\overline{\tau}_N$ , and  $\overline{T}_V$  on  $\dot{y}$  is shown in Figs. 10–12. These results were obtained by time-averaging during the time period in which the flows were in a steady-state, as defined above. It is evident and somewhat surprising that all these normalized stresses depend almost exactly linearly on  $\dot{y}$ .

As mentioned earlier, it was observed that for  $\dot{\gamma} = 5.9 \text{ s}^{-1}$  and  $\dot{\gamma} = 6.7 \text{ s}^{-1}$ , the total stress  $T_V$  exhibited an oscillatory behavior for t greater than  $\approx 30$  s. To determine the frequency content of these

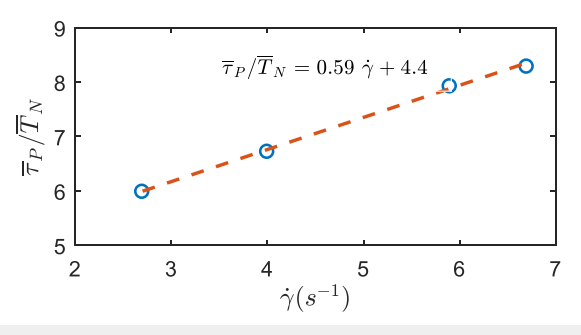


**FIG. 11.**  $\overline{\tau}_P/\overline{T}_N$  for shear rates  $\dot{y}$  = 2.7 s<sup>-1</sup>, 4.0 s<sup>-1</sup>, 5.9 s<sup>-1</sup>, and 6.7 s<sup>-1</sup>. The equation of the line fit used is  $\overline{\tau}_P/\overline{T}_N = 0.59\dot{y} + 4.4$ . The coefficient of determination is  $R^2$  = 0.9971.

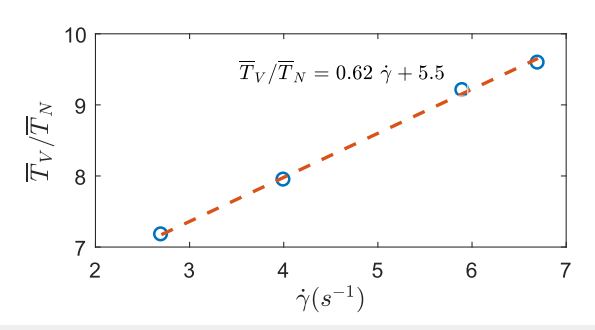


**FIG. 12.**  $\overline{T}_V/\overline{T}_N$  for shear rates  $\dot{\gamma}$  = 2.7 s<sup>-1</sup>, 4.0 s<sup>-1</sup>, 5.9 s<sup>-1</sup>, and 6.7 s<sup>-1</sup>. The equation of the line fit used is  $\overline{T}_V/\overline{T}_N = 0.62\dot{\gamma} + 5.5$ . The coefficient of determination is  $R^2$  = 0.9982.

oscillations, the Fourier spectral densities of the time series in these two cases were computed, and the results are shown in Fig. 13. These results show that in the case of  $\dot{\gamma}=6.7~\text{s}^{-1}$ , the spectral density shows a clear maximum at  $\approx 10^{-1}$  Hz. There also appears to be a secondary peak at  $\approx 2\times 10^{-1}$  Hz, which we interpret as the harmonic of the dominant frequency. For  $\dot{\gamma}=5.9~\text{s}^{-1}$ , a maximum in the spectral density is apparent at  $\approx 6\times 10^{-2}$  Hz. It is important to note that in the experiments of Groisman and Steinberg, the spectral density of the velocity fluctuations also exhibited spectral density peaks for these shear rates in good agreement with our results. Consistent with our results, they also observed that the peak frequency increased as the shear rate increased.

#### B. Ramp-up simulation

We have also performed a so-called ramp-up simulation. In this simulation, the rotation rate of the top plate was allowed to vary linearly in time as  $\Omega=0.005$  52t. In Fig. 14, the results of this simulation are shown in a plot of the normalized total stress  $T_V$  vs the shear rate  $\dot{y}$ . It is evident from these results that there is a transition period during which the stress rises rapidly. Subsequently, for  $\dot{y}>3$  s<sup>-1</sup>, a linear variation of the stress as a function of  $\dot{y}$  was observed.

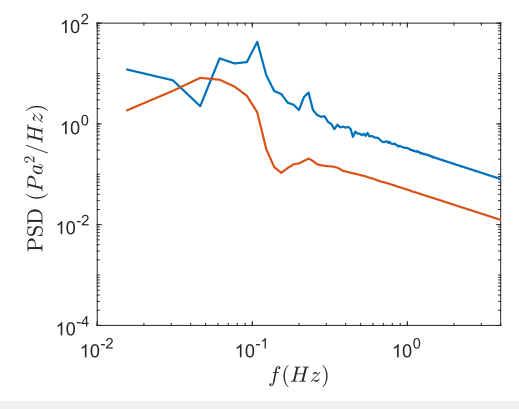


**FIG. 13**. The power spectral density (PSD) of  $T_V$  for shear rates  $\dot{y}=5.9~{\rm s}^{-1}$ , and  $6.7~{\rm s}^{-1}$ . The curves for these shear rates are given, respectively, by the colors red and blue.

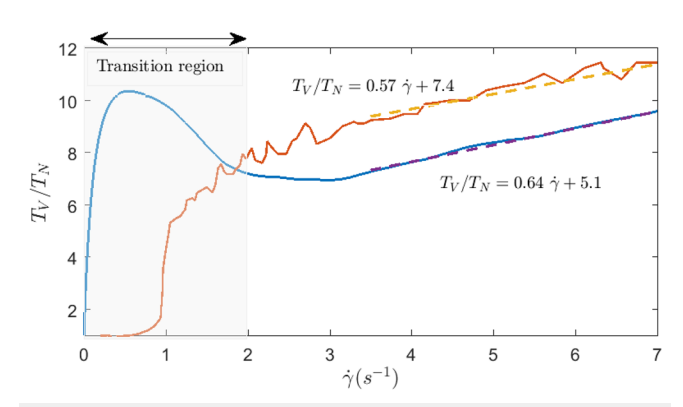


**FIG. 14.** The normalized total stress on the rotating plate,  $T_V/T_N$ , as a function of shear rate  $\dot{\gamma}$  from the experiments of Groisman and Steinberg (red) and the current simulation (blue) for a ramp-up scenario. Shown in the figure is a region of transition that appears at the lowest shear rates for both simulations and experiments. In the simulations, the shear rate  $\dot{\gamma}=0.021t$  which corresponds to  $\Omega=0.005\,52t$ .

Groisman and Steinberg<sup>1</sup> also performed a ramp-up experiment similar to our simulation. However, as far as we are aware, they did not specify the rate of increase of the rotation rate. These experiments also exhibit a transition period as well as a region in which the stress varies linearly with  $\dot{\nu}$ . As shown in Fig. 14, we observe a very close agreement between the slope of the linear region in our simulation and those of the experiments. However, we observe some differences, for example, the behavior of the experiments vs simulation is different in the transition region, and the magnitude of the stress ratio is  $\approx 30\%$  higher in the experiments. In Fig. 15, the evolution of stress components  $\tau_P$  and  $\tau_N$  is shown. It is evident from these results, as in the case of the constant  $\Omega$  simulations, that the polymeric component is the dominant component of the total stress on the top plate.

#### C. Flow visualizations

Insight into the nature of the stresses on the top plate can be gained by visualizing their spatial distribution as well as the relationship of these stresses to the velocity field. In order to do this, we have chosen to examine the case in which  $\dot{\gamma}=6.7~{\rm s}^{-1}$ . All the

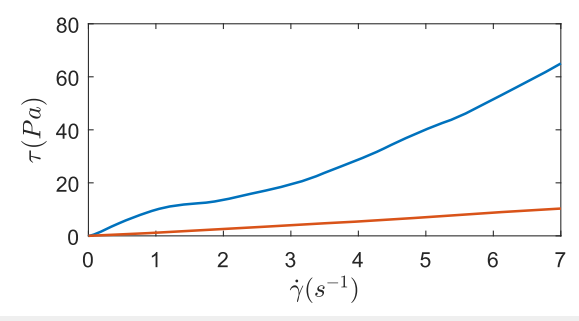


**FIG. 15.** The evolution of the polymeric stress component  $\tau_P$  (blue) and Newtonian stress component  $\tau_N$  (red) on the rotating plate in the ramp-up scenario.

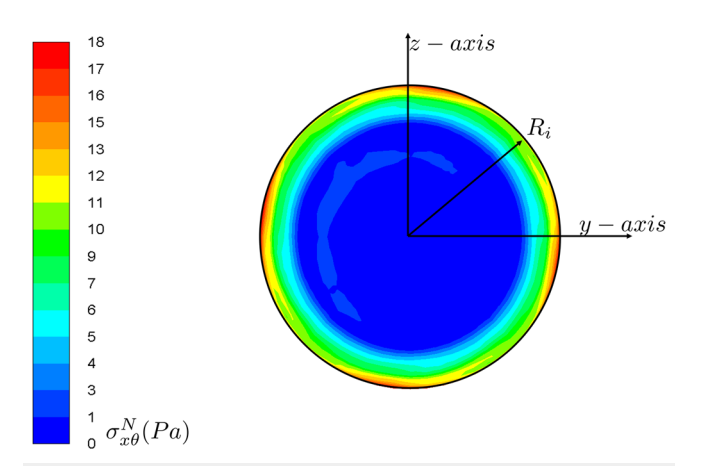


**FIG. 16.** Contour plot of the Newtonian stress,  $\sigma_{x\theta}^N$ , on the rotating plate for  $\dot{\gamma} = 6.7 \text{ s}^{-1}$ . These results were obtained from a random snapshot taken in the steady-state from simulations performed using a constant  $\Omega$ .

representations of the flow and the stresses shown in this subsection were obtained at the same time instant.

We note that the only component of the stress tensor that contributes to the torque on the top plate is  $\sigma_{x\theta}$ , the instantaneous stress on the top plate in the  $\hat{\theta}$  direction. In Figs. 16 and 17, we show the distribution of the Newtonian and polymeric components of this stress,  $\sigma_{x\theta}^N$  and  $\sigma_{x\theta}^P$ . At the instant shown, the flow was in an oscillatory steady-state, as mentioned earlier. We note that  $\sigma_{x\theta}^N$  exhibits a maximum value at the very edge of the top plate. This contrasts significantly with the distribution of the polymeric stress,  $\sigma_{x\theta}^P$ , which exhibits, surprisingly, its maximum value at a radius smaller than that of the top plate itself. It should be recalled that  $\sigma_{x\theta}^P$  is the major contributor to the torque on the top plate. In Fig. 18, we show the distribution of tr(C) on the top plate, which exhibits a maximum at the edge of the top plate similar to the distribution shown for

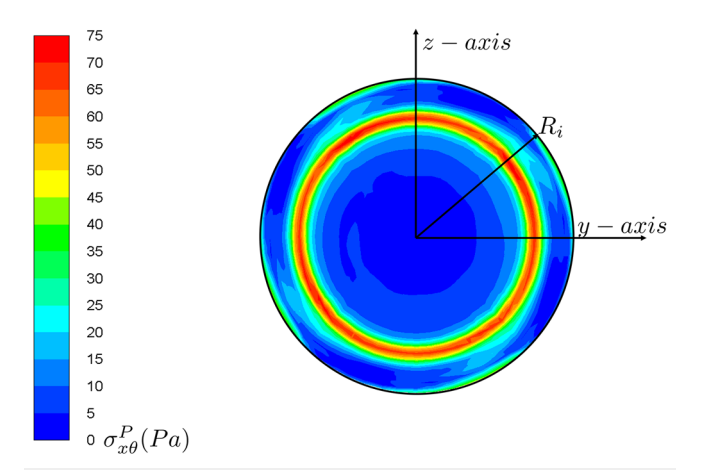


**FIG. 17.** Contour plot of the polymeric stress,  $\sigma^p_{x\theta}$ , on the rotating plate for  $\dot{\gamma}=6.7~\text{s}^{-1}$ . These results were obtained from a random snapshot taken in the steady-state from simulations performed using a constant  $\Omega$ .

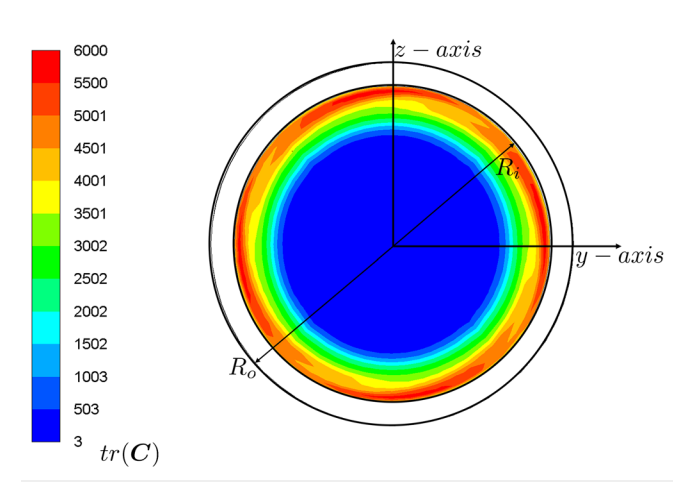


**FIG. 18.** Contour plot of the  $tr(\mathbf{C})$  on the rotating plate for  $\dot{\gamma}=6.7~\text{s}^{-1}$ . These results were obtained from a random snapshot taken in the steady-state from simulations performed using a constant  $\Omega$ .

 $\sigma_{x\theta}^{N}$ . Since  $\sqrt{tr(C)}$  can be thought of as a measure of the polymeric length, it is interesting to note that the torque on the top plate is primarily due to stresses (e.g.,  $\sigma_{x\theta}^{P}$ ) that do not correspond to regions where the polymers are maximally extended.

It is important to gain some insight into the relationship between the stresses on the rotating plate and the underlying flow kinematics. Before proceeding with this discussion, it is important to keep in mind that the main flow in this system is due to the rotation of the top plate that generates, due to the no-slip condition, a velocity field  $u_{\theta}$  whose time averaged value is  $\overline{u}_{\theta}(x,r)$ . In Fig. 19, a typical snapshot of the velocity field in a plane containing the x axis, which will also be referred to as the side view of the flow, is shown. We note that only the  $u_r$  and  $u_x$  components of the velocity vectors are shown in this plane. There are three features of the flow that are of particular importance. The first is the existence of a secondary flow, which manifests itself as a toroidal vortex, a vortex that extends circumferentially around the container. Although this is an instantaneous snapshot of the flow, the toroidal vortex is

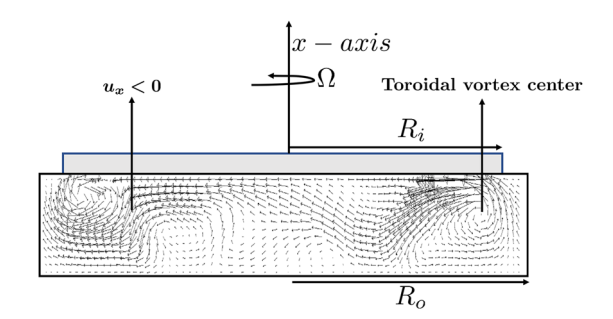


**FIG. 19.** Side view (x–y plane) of the velocity vector field for  $\dot{\gamma}=6.7~\text{s}^{-1}$ . The velocity field has been obtained at an arbitrary instant of time when the flow attained a statistically steady-state. Here, we indicate the position of the toroidal vortex and also a region associated with the vortex that gives rise to a negative vertical velocity.

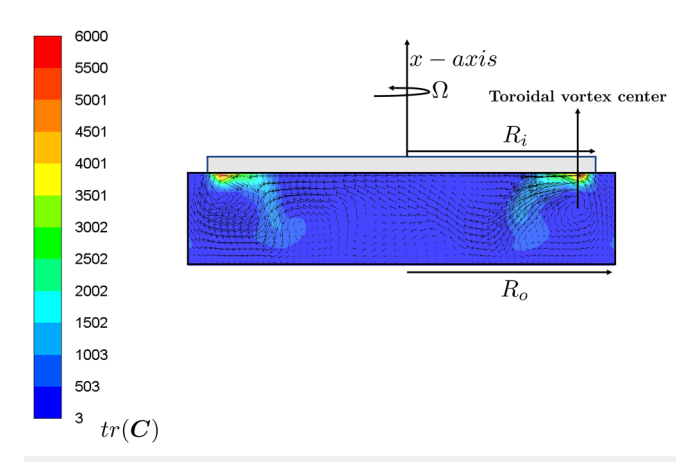


**FIG. 20.** Side view (x–y plane) of the contours of  $tr(\mathbf{C})$  overlaid on the velocity vector field at  $\dot{y}=6.7~\mathrm{s}^{-1}$ . The velocity field and  $tr(\mathbf{C})$  have been obtained at an arbitrary instant of time when the flow attained a statistically steady-state.

a long-lasting coherent structure, which appears in every simulation we have performed in this work. Second, we point out in this figure the regions near the top plate in which  $u_x < 0$ , denoting that fluid particles are descending from the top plate into the interior of the flow. It is evident from the vector field that this region of descending fluid is directly correlated with the flow field associated with the toroidal vortex. Finally, it is clear that the flow field lacks symmetry in the xy-plane.

In Fig. 20, we show the contours of tr(C) overlaid upon the velocity field shown in the previous figure. It is clear from this that the maximum value of tr(C) occurs at the edge of the rotating plate. Since the highest velocity gradients occur at the edge of the plate, we would expect the highest rate of polymeric stretching to occur there. It is, therefore, reasonable to expect tr(C) to be maximal in this region. In Fig. 21, we plot the stress  $\sigma_{x\theta}^P$  overlaid upon the velocity vector field. It is evident that the maximum value

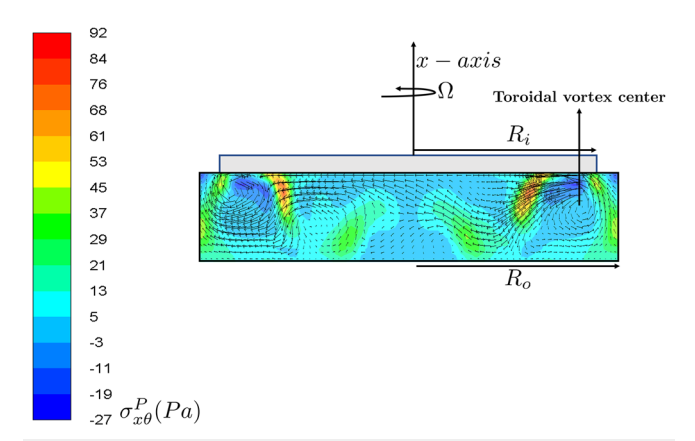


**FIG. 21.** Side view (*x*–*y* plane) of the contours of  $\sigma^P_{x\theta}$  overlaid on the velocity vector field at  $\dot{y}=6.7~{\rm s}^{-1}$ . The velocity field and  $\sigma^P_{x\theta}$  have been obtained at an arbitrary instant of time when the flow attained a statistically steady-state.

of  $\sigma_{x\theta}^P$  occurs near the rotating plate and that these regions of high  $\sigma_{x\theta}^P$  are highly correlated with regions of the flow where fluid particles are descending into the interior. From a heuristic point of view, we can envision that in this region of downward flow, a polymer molecule would be stretched in the  $\theta$ -direction. This is directly due to the existence of the mean velocity  $\overline{u}_{\theta}(x,r)$  since we can envision that the end of the molecule closer to the top plate moves in the  $\theta$ -direction faster than the end of the molecule farther from the top plate. This appears to explain the observation that  $\sigma_{x\theta}^P$  exhibits a maximum value at a radius smaller than  $R_i$ , as previously indicated in Fig. (17).

#### V. DISCUSSION

The experiments of Groisman and Steinberg<sup>1</sup> uncovered a new phenomenon called elastic turbulence, which appeared in the swirling flow of a dilute polymer solution driven by a rotating plate. In these experiments, the gross properties of the flow could be characterized by measuring the torque on the rotating plate. This torque was found in the experiments to be approximately one order of magnitude greater than the corresponding torque in the flow of a Newtonian fluid. In the current work, we have employed a DNS of the exact same flow with comparable fluid properties and geometry. The FENE-P model was used as a theoretical basis for describing the polymer dynamics. The complete model was implemented using the ANSYS-FLUENT platform, and the log-conformation model was used to overcome the high Weissenberg number problem. DNS methods such as the one used in this study can provide detailed information that would be difficult to obtain experimentally. For example, simulations can determine the entire velocity field in space time, the internal stresses in the fluid, and the stresses on bounding surfaces. The relationship between the velocity field and the stress field can be also investigated. The opportunity to utilize the simulation methods described herein to more deeply investigate this flow provided the primary motivation for this work.

Two kinds of simulations were performed, namely, a series of constant- $\Omega$  simulations and a ramp-up simulation. In the constant- $\Omega$  simulations, it was found that the major contributor to the torque was the polymeric stress  $\tau_P$  that was typically about 5 times greater than the Newtonian stress  $\tau_N$ . In addition, quasi-periodic oscillations of the torque dominated by one frequency were found for the highest  $\Omega$  values. The frequency content of these oscillations was in reasonable agreement with the experiments of Groisman and Steinberg. In the ramp-up simulation, we observed a transient period in which the stress rose rapidly followed by a period where the normalized total stress increased linearly with  $\dot{y}$ . The rate at which the total normalized stress increased was found to be in good agreement with the experiments.

Flow visualizations were used to gain insight into the relationship between the flow kinematics and the stress field. The stress distribution on the rotating plate as well as the side view of the velocity field was obtained simultaneously. The side view of the velocity field revealed the existence of a toroidal vortex, which exists in the vicinity of the outer edge of the rotating plate. It was found that  $\operatorname{tr}(C)$  is maximal at the edge of the rotating plate, whereas the polymeric stress maximum was found closer to the center of the plate. It was argued that the position of maximum polymeric stress could be related directly to a downward flow caused by the toroidal vortex.

While we discussed the similarities between our simulations and experiments, it is important to point out several differences between them. In particular, while the experiments achieved a chaotic flow state both in space and time, it is unclear that our simulations have achieved a similar state. However, the simulated flow did exhibit quasi-periodic behavior in time and also spatial asymmetry, which are some of the characteristics of turbulence. On the other hand, if the simulated flow was of a turbulent nature, it is most likely not a strong turbulence. Instead, it seems to us that the flow achieved a state that could be transitional between laminar and turbulent states. We should also point out other differences. In the simulations, the total stress on the top plate was found to be somewhat smaller than that found in the experiments. In addition, the frequency distribution of the stress fluctuations was found not to be as broad as reported in the experiments. The resolution of many of these issues will certainly require a greater experimental effort. More specifically, a detailed mapping of the internal velocity field will be especially illuminating. For example, it will be important to determine if the toroidal vortex found in our simulations, which was largely responsible for the particular characteristics of the stress distribution on the top plate, actually exists in the real flow.

#### **ACKNOWLEDGMENTS**

R.A.H. received support from the National Science Foundation under Grant No. 1904953. The authors also acknowledge useful discussions with K. R. Rajagopal.

## APPENDIX: LIST OF SIMULATION PARAMETERS

**TABLE II.** A complete list of all simulations performed in this work is shown below. For each run, we list the angular velocity of the plate,  $\Omega$ , the shear rate,  $\dot{\gamma}$  ( s<sup>-1</sup>), the Reynolds number, Re, and the Weissenberg number, Wi.

Run no.	$\Omega \left( s^{-1}\right)$	$\dot{y}$ (s <sup>-1</sup> )	Re	Wi
1	0.263 158	1	1	3.4
2	0.315789	1.2	1.2	4.08
3	0.368 421	1.4	1.4	4.76
4	0.421 053	1.6	1.6	5.44
5	0.473684	1.8	1.8	6.12
6	0.526316	2	2	6.8
7	0.578947	2.2	2.2	7.48
8	0.631 579	2.4	2.4	8.16
9	0.684211	2.6	2.6	8.84
10	0.736842	2.8	2.8	9.52
11	0.789474	3	3	10.2
12	0.842 105	3.2	3.2	10.88
13	0.894737	3.4	3.4	11.56
14	0.947 368	3.6	3.6	12.24
15	1	3.8	3.8	12.92
16	1.052632	4	4	13.6
17	1.473 684	5.6	5.6	19.04
18	1.763 158	6.7	6.7	22.78

#### **DATA AVAILABILITY**

The data that support the findings of this study are available within the article.

#### **REFERENCES**

- <sup>1</sup> A. Groisman and V. Steinberg, "Elastic turbulence in a polymer solution flow," Nature **405**, 53–55 (2000).
- <sup>2</sup>B. Toms, in *Proceedings of the 1st International Congress on Rheology* (North Holland, Amsterdam, 1949), Vol. II, p. 135.
- <sup>3</sup>P. S. Virk, "Drag reduction fundamentals," AIChE J. 21, 625–656 (1975).
- <sup>4</sup>C. M. White and M. G. Mungal, "Mechanics and prediction of turbulent drag reduction with polymer additives," Annu. Rev. Fluid Mech. **40**, 235–256 (2008).
- $^5\mathrm{J}$  . L. Lumley, "Drag reduction by additives," Annu. Rev. Fluid Mech. 1, 367–384 (1969).
- <sup>6</sup>J. R. A. Pearson, "Instability in non-Newtonian flow," Annu. Rev. Fluid Mech. **8**, 163–181 (1976).
- <sup>7</sup>C. J. S. Petrie and M. M. Denn, "Instabilities in polymer processing," AIChE J. **22**, 209–236 (1976).
- <sup>8</sup>R. G. Larson, "Instabilities in viscoelastic flows," Rheol. Acta 31, 213–263 (1992).
  <sup>9</sup>G. H. McKinley, P. Pakdel, and A. Öztekin, "Rheological and geometric scaling of purely elastic flow instabilities," J. Non-Newtonian Fluid Mech. 67, 19–47 (1996).
- $^{10}$ B. M. Baumert and S. J. Muller, "Flow visualization of the elastic Taylor-Couette instability in Boger fluids," Rheol. Acta **34**, 147–159 (1995).
- <sup>11</sup>M. D. Graham, "Effect of axial flow on viscoelastic Taylor-Couette instability," J. Fluid Mech. 360, 341–374 (1998).
- <sup>12</sup>P. Pakdel and G. H. McKinley, "Elastic instability and curved streamlines," Phys. Rev. Lett. **77**, 2459 (1996).
- <sup>13</sup>N. Phan-Thien, "Coaxial-disk flow of an Oldroyd-B fluid: Exact solution and stability," J. Non-Newtonian Fluid Mech. 13, 325–340 (1983).
- <sup>14</sup>N. Phan-Thien, "Cone-and-plate flow of the Oldroyd-B fluid is unstable," J. Non-Newtonian Fluid Mech. 17, 37–44 (1985).
- <sup>15</sup>G. H. McKinley, J. A. Byars, R. A. Brown, and R. C. Armstrong, "Observations on the elastic instability in cone-and-plate and parallel-plate flows of a polyisobutylene Boger fluid," J. Non-Newtonian Fluid Mech. 40, 201–229 (1991).
- <sup>16</sup>G. H. Mckinley, A. Öztekin, J. A. Byars, and R. A. Brown, "Self-similar spiral instabilities in elastic flows between a cone and a plate," J. Fluid Mech. **285**, 123–164 (1995).
- <sup>17</sup>J. A. Byars, A. Öztekin, R. A. Brown, and G. H. Mckinley, "Spiral instabilities in the flow of highly elastic fluids between rotating parallel disks," J. Fluid Mech. **271**, 173–218 (1994).
- <sup>18</sup>G. H. McKinley, R. C. Armstrong, and R. Brown, "The wake instability in viscoelastic flow past confined circular cylinders," Philos. Trans. R. Soc. London, Ser. A 344, 265–304 (1993).
- $^{19}$ M. D. Graham, "Interfacial hoop stress and instability of viscoelastic free surface flows," Phys. Fluids 15, 1702–1710 (2003).
- <sup>20</sup> K. A. Kumar and M. D. Graham, "Buckling instabilities in models of viscoelastic free surface flows," J. Non-Newtonian Fluid Mech. 89, 337–351 (2000).
- <sup>21</sup> H. Tennekes and J. L. Lumley, A First Course in Turbulence (MIT press, 1972).
- <sup>22</sup>T. Burghelea, E. Segre, and V. Steinberg, "Role of elastic stress in statistical and scaling properties of elastic turbulence," Phys. Rev. Lett. **96**, 214502 (2006).
- <sup>23</sup>T. Burghelea, E. Segre, and V. Steinberg, "Elastic turbulence in von Karman swirling flow between two disks," Phys. Fluids 19, 053104 (2007).
- <sup>24</sup>A. Groisman and V. Steinberg, "Elastic turbulence in curvilinear flows of polymer solutions," New J. Phys. 6, 29 (2004).
- <sup>25</sup> A. Groisman and V. Steinberg, "Efficient mixing at low Reynolds numbers using polymer additives," Nature **410**, 905–908 (2001).
- <sup>26</sup>T. Burghelea, E. Segre, I. Bar-Joseph, A. Groisman, and V. Steinberg, "Chaotic flow and efficient mixing in a microchannel with a polymer solution," Phys. Rev. E **69**, 066305 (2004).
- <sup>27</sup>Y. Jun and V. Steinberg, "Elastic turbulence in a curvilinear channel flow," Phys. Rev. E 84, 056325 (2011).

- <sup>28</sup> L. Pan, A. Morozov, C. Wagner, and P. E. Arratia, "Nonlinear elastic instability in channel flows at low Reynolds numbers," Phys. Rev. Lett. 110, 174502 (2013).
- <sup>29</sup>B. Qin and P. E. Arratia, "Characterizing elastic turbulence in channel flows at low Reynolds number," Phys. Rev. Fluids **2**, 083302 (2017).
- <sup>30</sup>R. Fattal and R. Kupferman, "Constitutive laws for the matrix-logarithm of the conformation tensor," J. Non-Newtonian Fluid Mech. **123**, 281–285 (2004).
- <sup>31</sup>S. Berti, A. Bistagnino, G. Boffetta, A. Celani, and S. Musacchio, "Two-dimensional elastic turbulence," Phys. Rev. E 77, 055306 (2008).
- 32 S. Berti and G. Boffetta, "Elastic waves and transition to elastic turbulence in a two-dimensional viscoelastic Kolmogorov flow," Phys. Rev. E 82, 036314 (2010).
- <sup>33</sup>Z. Hong-Na, L. Feng-Chen, C. Yang, K. Tomoaki, and Y. Bo, "Direct numerical simulation of elastic turbulence and its mixing-enhancement effect in a straight channel flow," Chin. Phys. B **22**, 024703 (2013).
- <sup>34</sup>N. Liu and B. Khomami, "Elastically induced turbulence in Taylor-Couette flow: Direct numerical simulation and mechanistic insight," J. Fluid Mech. 737, R4 (2013).
- 35 T. Von Kármán, "Über laminare und turbulente reibung," Z. Angew. Math. Mech. 1, 233–252 (1921).
- <sup>36</sup>P. Mitschka, "Nicht-Newtonsche flüssigkeiten II. Drehströmungen Ostwald-de Waelescher nicht-Newtonscher flüssigkeiten," Collect. Czech. Chem. Commun. 29, 2892–2905 (1964).
- <sup>37</sup>P. D. Ariel, "On the flow of an elastico-viscous fluid near a rotating disk," J. Comput. Appl. Math. 154, 1–25 (2003).
- <sup>38</sup>J. R. Stokes, L. J. W. Graham, and D. V. Boger, "Vortex breakdown in confined swirling flow of a dilute flexible polymer solution," Proc. XIIth Int. Congr. on Rheol. Laval University, Quebec City, Canada, 1996, edited by A. Ait-Kadi, J. M. Dealy, D. F. James, and M. C. Williams (1996), pp. 359–360.
- <sup>39</sup>D. V. Boger, "A highly elastic constant-viscosity fluid," J. Non-Newtonian Fluid Mech. 3, 87–91 (1977).
- <sup>40</sup>J. C. Maxwell, "IV. On the dynamical theory of gases," Philos. Trans. R. Soc. London 157, 49–88 (1867).
- <sup>41</sup> H. R. Warner, Jr, "Kinetic theory and rheology of dilute suspensions of finitely extendible dumbbells," Ind. Eng. Chem. Fundam. 11, 379–387 (1972).
- <sup>42</sup>R. B. Bird and H. R. Warner, Jr, "Hydrodynamic interaction effects in rigid dumbbell suspensions. I. Kinetic theory," Trans. Soc. Rheol. **15**, 741–750 (1971).
- <sup>43</sup>R. B. Bird, P. J. Dotson, and N. L. Johnson, "Polymer solution rheology based on a finitely extensible bead-spring chain model," J. Non-Newtonian Fluid Mech. 7, 213–235 (1980).
- <sup>44</sup>R. B. Bird, R. C. Armstrong, and O. Hassager, *Dynamics of Polymeric Liquids*, Fluid Mechanics (Wiley, 1987), Vol. 1.
- <sup>45</sup>R. I. Tanner, *Engineering Rheology* (OUP Oxford, 2000), Vol. 52.
- <sup>46</sup>I. Ghosh, G. H. McKinley, R. A. Brown, and R. C. Armstrong, "Deficiencies of FENE dumbbell models in describing the rapid stretching of dilute polymer solutions," J. Rheol. 45, 721–758 (2001).
- <sup>47</sup>R. Sureshkumar, A. N. Beris, and R. A. Handler, "Direct numerical simulation of the turbulent channel flow of a polymer solution," Phys. Fluids **9**, 743–755 (1997).
- <sup>48</sup>C. D. Dimitropoulos, R. Sureshkumar, and A. N. Beris, "Direct numerical simulation of viscoelastic turbulent channel flow exhibiting drag reduction: Effect

- of the variation of rheological parameters," J. Non-Newtonian Fluid Mech. **79**, 433–468 (1998).
- <sup>49</sup>C. D. Dimitropoulos, R. Sureshkumar, A. N. Beris, and R. A. Handler, "Budgets of Reynolds stress, kinetic energy and streamwise enstrophy in viscoelastic turbulent channel flow," Phys. Fluids 13, 1016–1027 (2001).
- <sup>50</sup> R. A. Handler, K. D. Housiadas, and A. N. Beris, "Karhunen-Loeve representations of turbulent channel flows using the method of snapshots," Int. J. Numer. Methods Fluids **52**, 1339–1360 (2006).
- <sup>51</sup> M. Masoudian, K. Kim, F. T. Pinho, and R. Sureshkumar, "A Reynolds stress model for turbulent flow of homogeneous polymer solutions," Int. J. Heat Fluid Flow **54**, 220–235 (2015).
- <sup>52</sup>S. Azad, H. A. Moghadam, A. Riasi, and H. M. Darian, "Numerical simulation of a viscoelastic RANS turbulence model in a diffuser," Korea-Aust. Rheol. J. 30, 249–260 (2018).
- <sup>53</sup>S. Azad, A. Riasi, H. Amiri Moghadam *et al.*, "Parametric study of a viscoelastic RANS turbulence model in the fully developed channel flow," J. Comput. Appl. Mech. 48, 65–74 (2017).
- $^{54}$ P. R. Resende, A. M. Afonso, and D. O. Cruz, "An improved k-ε turbulence model for FENE-P fluids capable to reach high drag reduction regime," Int. J. Heat Fluid Flow 73, 30–41 (2018).
- <sup>55</sup>E. Rasti, F. Talebi, and K. Mazaheri, "A turbulent duct flow investigation of drag-reducing viscoelastic FENE-P fluids based on different low-Reynolds-number models," Physica A 526, 120718 (2019).
- <sup>56</sup>P. R. Resende and A. S. Cavadas, "New developments in isotropic turbulent models for FENE-P fluids," Fluid Dyn. Res. 50, 025508 (2018).
- <sup>57</sup>K. Kim and R. Sureshkumar, "Effects of polymer stresses on analogy between momentum and heat transfer in drag-reduced turbulent channel flow," Phys. Fluids 30, 035106 (2018).
- <sup>58</sup>H. M. Xia, S. Y. M. Wan, C. Shu, and Y. T. Chew, "Chaotic micromixers using two-layer crossing channels to exhibit fast mixing at low Reynolds numbers," Lab Chip 5, 748–755 (2005).
- <sup>59</sup> R. A. Handler, E. Blaisten-Barojas, P. M. Ligrani, P. Dong, and M. Paige, "Vortex generation in a finitely extensible nonlinear elastic Peterlin fluid initially at rest," Eng. Rep. 2, e12135 (2020).
- <sup>60</sup>E. S. G. Shaqfeh, "Purely elastic instabilities in viscometric flows," Annu. Rev. Fluid Mech. 28, 129–185 (1996).
- <sup>61</sup>T. Vaithianathan and L. R. Collins, "Numerical approach to simulating turbulent flow of a viscoelastic polymer solution," J. Comput. Phys. 187, 1–21 (2003).
- <sup>62</sup>R. Fattal and R. Kupferman, "Time-dependent simulation of viscoelastic flows at high Weissenberg number using the log-conformation representation," J. Non-Newtonian Fluid Mech. **126**, 23–37 (2005).
- <sup>63</sup> A. Afonso, P. J. Oliveira, F. T. Pinho, and M. A. Alves, "The log-conformation tensor approach in the finite-volume method framework," J. Non-Newtonian Fluid Mech. 157, 55–65 (2009).
- <sup>64</sup>F. Habla, M. W. Tan, J. Haßlberger, and O. Hinrichsen, "Numerical simulation of the viscoelastic flow in a three-dimensional lid-driven cavity using the log-conformation reformulation in OpenFOAM<sup>®</sup>," J. Non-Newtonian Fluid Mech. **212**. 47–62 (2014).